J Mater Sci (2020) 55:5135–5144

Electronic materials

Method of electron affinity evaluation for the type-2 InAs/InAs$_{1-x}$Sb$_x$ superlattice

Tetiana Manyk[1,*], Krzysztof Murawski[1], Krystian Michalczewski[2], Kacper Grodecki[1], Jaroslaw Rutkowski[1], and Piotr Martyniuk[1]

[1] Institute of Applied Physics, Military University of Technology, 2 Kaliskiego Str., 00-908 Warsaw, Poland
[2] VIGO System S.A., 129/133 Poznanska Str., 05-850 Ozarow Mazowiecki, Poland

Received: 27 September 2019
Accepted: 3 January 2020
Published online: 23 January 2020

ABSTRACT

The type-2 InAs/InAs$_{1-x}$Sb$_x$ superlattices on GaAs substrate with GaSb buffer layer were investigated by comparison of theoretical simulations and experimental data. The algorithm for selection of input parameters (binary and ternary materials) for simulations is presented. We proposed the method of the bandgap energy extraction of the absorption curve. The correct choice of the bulk materials and bowing parameters for the ternary alloys allows to reach good agreement of the experimental data and theoretical approach. One of the key achievements of this work was an electron affinity assessment for the device's theoretical simulation. The detectivity of the long-/very long-wave InAs/InAs$_{1-x}$Sb$_x$ superlattice photoconductors at the level of $\sim 8 \times 10^9$ cm Hz$^{1/2}$/W (cutoff wavelength 12 μm) and $\sim 9 \times 10^8$ cm Hz$^{1/2}$/W (cutoff wavelength 18 μm) at a temperature 230 K confirmed the good quality of these materials.

Introduction

The InAs/GaSb and InAs/InAs$_{1-x}$Sb$_x$ superlattices (SLs) have been considered as an alternative to HgCdTe. These materials were first presented by Smith et al. in 1987 initiating the process of the HgCdTe use for infrared (IR) applications [1–4]. Recently, researchers have focused on the fact that InAs/InAs$_{1-x}$Sb$_x$ SLs are more flexible in the optimization of device performance. The type-2 superlattices (T2SLs) InAs/InAs$_{1-x}$Sb$_x$ are used for the fabrication of barrier detectors to include nBn and pBn design [5, 6], low-noise interband cascade infrared photodetectors (ICIP) [7, 8], and avalanche photodiodes (APD) [9], for wide range of applications in the field of science, medicine, technology, safety, industry, medical diagnostic imaging, night vision devices, and spectroscopy.

Figure 1 shows the bandgap (E_g) dependence on the lattice constant (a) for bulk A^3B^5 materials (InAs, InSb, GaSb, and GaAs) being used for SLs fabrication. In the case of the ternary materials, Vegard's law was used to determine lattice constant [10–12].

The GaSb has a similar lattice constant to InAs and InSb, while the GaAs exhibits a large lattice mismatch in comparison with the mentioned materials leading to the high strains. When growing a SL, it was

Address correspondence to E-mail: tetjana.manyk@wat.edu.pl

https://doi.org/10.1007/s10853-020-04347-6

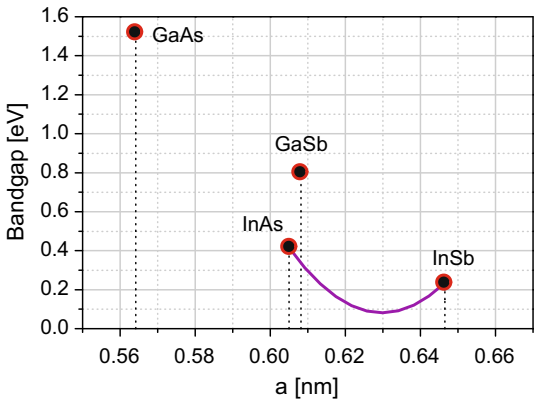

Figure 1 Lattice constant and bandgap of the bulk A^3B^5 materials at $T = 0$ K.

important to reduce the tension between the SL constituting layers and the substrate on which the SL was deposited. That is why it is important to choose the buffer layer and minimal thickness (with reference to the thickness of the SL) in which the tension between the SL and the buffer layer was averaged. As a result, the proper buffer layer selection reduced the dislocations density having a great influence on the characteristics of the processed detectors. We decided to apply the interfacial misfit array (IMF) technique in order to get a defect-free buffer layer.

In this work, a numerical modeling by APSYS platform of medium wavelength infrared (MWIR) and long wavelength infrared (LWIR) T2SLs InAs/$InAs_{1-x}Sb_x$ IR structure is presented. In the simulation, the strains created by GaSb buffer in InAs and $InAs_{1-x}Sb_x$ layers were considered. It was shown that the use of T2SLs InAs/$InAs_{1-x}Sb_x$ with the "strain-balanced" condition makes it possible to grow high-quality SLs for IR applications.

T2SL InAs/$InAs_{1-x}Sb_x$ structure

The InAs/InAsSb T2SLs were grown on semi-insulating GaAs (001) substrates with 2° offcut toward <110> in RIBER Compact 21-DZ solid-source molecular beam epitaxy (MBE) system. The substrates were thermally deoxidized, and a 250-nm-thick GaAs layer was deposited at 665 °C in order to smooth the surface after deoxidization. Then, a 1.2-μm-thick GaSb layer was grown using IMF technique to reduce the large lattice mismatch between GaAs substrate and the SLs. Finally, a 300–450 periods, non-intentionally doped InAs/$InAs_{1-x}Sb_x$ T2SL absorber layer, were deposited at 425 °C. The growth processes have been monitored in situ by RHEED system. The T2SL InAs/$InAs_{1-x}Sb_x$ structure is presented in Fig. 2. The n describes the number of SL periods, and L is the thickness of SL components. Detailed description of the T2SLs growth procedure is given in [13].

High-resolution X-ray diffraction (PANalytical X'Pert) was utilized to assess the structural and crystallographic properties of the grown samples. The thickness of the several layers in SLs could be determined by the distance between the satellite peaks appearing on the radial scan. In order to know the antimony composition in InAsSb layer, the secondary ion mass spectrometry (SIMS) was used. The PL emission was analyzed using a Bruker Vertex v70 Fourier transform infrared (FTIR) spectrometer to determine the bandgap energy of the InAs/InAsSb T2SLs absorber. Table 1 presents the basic parameters of the grown samples.

All samples were checked for compliance with the "strain-balanced" condition [14, 15]. This means that the strain occurring between the components of the SL (InAs and $InAs_{1-x}Sb_x$) and the buffer layers (GaSb) was small, not causing a large number of dislocations. Hence, the conclusion was made that these strains will not have a significant impact on the characteristics of the device.

The several expressions for designation of the compressive (L_{InAsSb}) and tensile (L_{InAs}) layer thickness have been used. An average lattice method arose from the notion that a "strain-balanced" structure could be reached by averaging of the compressive and tensile lattice parameters. This could be derived assuming identical elastic material properties (material elastic constants), and the balance equation is a form:

$$a_{GaSb} \cdot (L_{InAs} + L_{InAsSb}) = a_{InAs} \cdot L_{InAs} + a_{InAsSb} \cdot L_{InAsSb}, \quad (1)$$

where a_i is the lattice constant of "i" materials.

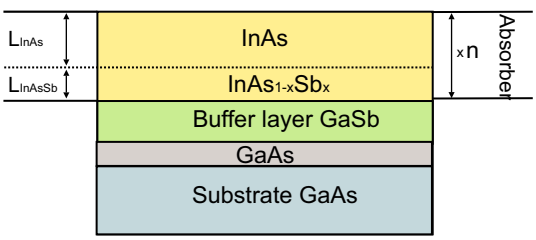

Figure 2 Schematic representation of the T2SL InAs/$InAs_{1-x}Sb_x$ structure.

Table 1 The T2SLs parameters: thickness L, Sb molar composition x_{Sb}, number of periods n

Sample	Sb molar composition x_{Sb}	L (nm)			Periods n
		L_{InAs}	L_{InAsSb}	$L_{InAs} + L_{InAsSb}$	
A^a	0.38	10.40	2.80	13.20	300
B^a	0.41	14.35	3.95	18.30	300
C	0.38	9.35	4.20	13.55	300
D	0.38	5.10	1.96	7.06	450
E	0.4	10.60	2.55	13.15	400
F^a	0.39	9.90	2.80	12.70	350
G^a	0.4	10.00	2.80	12.80	300

[a]Strain-balanced samples

The thickness of a "strain-balanced" structure for the samples presented in Table 1 was determined by the equation [14, 16]:

$$L_{InAsSb} = \left(\frac{L}{x_{Sb}}\right) \cdot \left(\frac{a_{GaSb} - a_{InAs}}{a_{InSb} - a_{InAs}}\right), \quad (2)$$

where L is the thickness of one SL period.

The next approach suggested that the "strain-balanced" structure could be reached by assuming equal thickness for the tensile and compressive layers. It could be assumed that the structure is balanced if the following condition is met [15–19]:

$$\epsilon_{xx}^{InAs} \cdot L_{InAs} + \epsilon_{xx}^{InAsSb} \cdot L_{InAsSb} = 0, \quad (3)$$

ϵ is the stresses related to the buffer layer.

In order to express the strain, the following equation was used:

$$L_{InAsSb} = L \cdot \left(\frac{a_{InAsSb} \cdot (a_{GaSb} \cdot a_{InAs})}{a_{GaSb} \cdot (a_{InAsSb} \cdot a_{InAs})}\right). \quad (4)$$

Comparison of these two equations suggested that the discrepancy in the thickness of the InAsSb layer was less than 5%, not causing significant changes in the devices performance. The sample satisfaction of the condition "strain-balanced" is marked by in the Table 1.

Theoretical simulation of the SLs optical characteristics

The commercial APSYS platform allowed to study the SLs optical characteristics. The 4 bands method (kp 8×8) with periodic boundary was used, which is well described in the papers [20–22]. In addition, to obtain symmetric wave functions $\Psi_{e(h)}$, the Kane parameter, $F = 0$ was assumed [22]. The standard value of $k = 0.06$ was used in simulations with the exception for the determination of the effective masses, for which the smaller interval of the vector $k = 0.03$ was applied. Up to date, many different values of the parameters required for the band structure theoretical modeling have been used. The parameters implemented in our calculations are presented in "Appendix" in Table 3 [20, 23–32].

The strain could also influence the band structure of the material. In our calculations, the solid-theory model was used [23, 24]. Figure 3 shows the SLs $InAs/InAs_{1-x}Sb_x$ band structure for unstrained and strained conditions. Electron affinity for unstrained materials InAs and InSb is presented in Table 3. Under the influence of strain, an electron affinity changed and the valence band splitted on the heavy and light holes subbands.

The set of dispersion curves $E = f(k, q)$, allowing to estimate electron and hole effective masses (heavy and light holes) for the SL, was simulated. The effective masses were consistent with those presented in [21]. Figure 4 shows the absorption coefficient (α) for three samples: *Sample-A*; *Sample-B*, and *Sample-D* with selected absorber thicknesses and x_{Sb}.

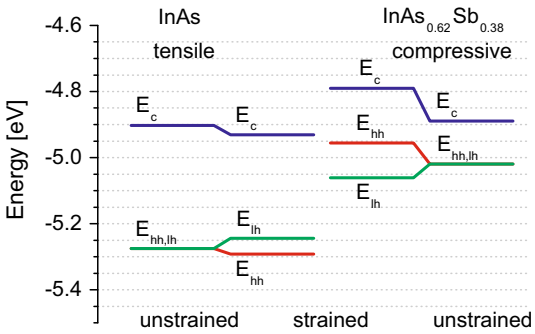

Figure 3 The energy band profiles of unstrained and strained SLs.

The presented "strain-balanced" structures, *Sample-A*; *Sample-B;* and *Sample-D*, were optimized for 12 μm, 18 μm, and 7 μm cutoff wavelengths, respectively. In comparison with the *MWIR* devices where $\alpha \approx 6000\ \mathrm{cm}^{-1}$, the *LWIR* detector absorption coefficient was less than $1500\ \mathrm{cm}^{-1}$. The sharp change in the absorption characteristics (e.g., *Sample-D*) was caused by two transitions: c_1–hh_1 and c_1–lh_1. This was presented in more detail in [21].

The correct determination of the SL energy gap could be reached by a derivative of the absorption coefficient which was shown for *Sample-C* at $T = 300$ K in Fig. 5. In this case, a derivative of the absorption coefficient on energy (this graph is shown upper left) had to be calculated in order to determine the maximum value.

Figure 6 represents a theoretical simulation of the absorption coefficients for *Sample-C* at selected temperatures 120 K, 180 K, 230 K, and 300 K. It can be seen that when temperature increased, the width of the bandgap decreased and the cutoff wavelength increased, correspondingly. Also, the maximum value of the absorption coefficient decreased with temperature.

In order to determine the T2SLs electron affinity χ (position of the conductivity band E_c), the band structure of one of the SL samples with period $L = 18.3$ nm and selected thicknesses of the InAs and $InAs_{1-x}Sb_x$ layers were simulated. Since APSYS platform gives only the relevant values of E_c, the simulated value was adjusted to that extracted from the linear relationship for the thickness L_{InAsSb} of the layer $InAs_{1-x}Sb_x$ corresponding to the "strain-balanced" structure.

Figure 7 shows the linear dependence of the SL electron affinity χ (red line) versus the thickness of the InAsSb layer and the theoretical simulation (black curve) intersecting at the point $L_{InAsSb} = 3.95$ nm corresponding to the balanced SL (see eq. 2). The different slope of these curves could be explained by additional strains between the layers when their thickness deviates from the thickness in the "strain-balanced" structure. For thicker InAsSb layers, the electron affinity was reduced, while for thinner ones it was higher than the linear averaging. Even though these changes were low, a 20% deviation from the "strain-balanced" thickness resulted in a reduction in electron affinity by 0.002 eV.

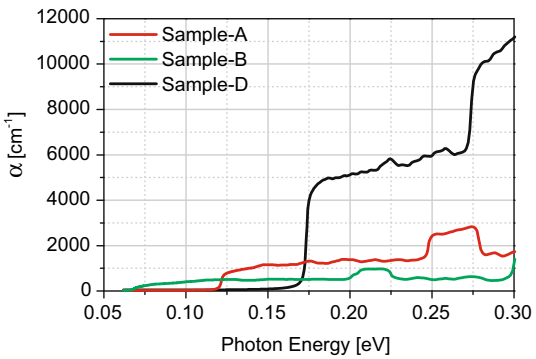

Figure 4 The simulated absorption coefficient versus photon energy at $T = 230$ K.

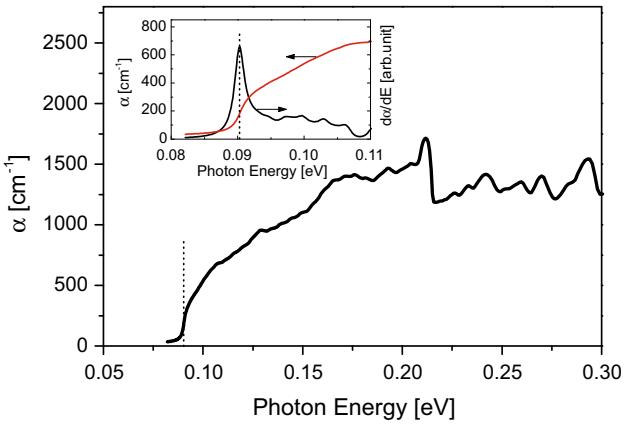

Figure 5 The simulated absorption coefficient at $T = 300$ K for *Sample-C* (method for the determining of the bandgap).

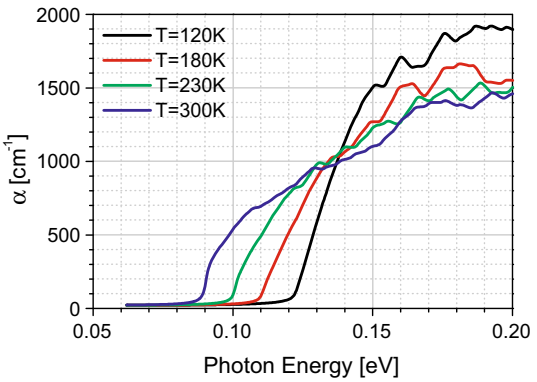

Figure 6 The simulated absorption coefficient versus temperature for *Sample-C*.

Results

In order to compare the simulated absorption curves (*Sample-C* at temperature $T = 220$ K) with the experimental data, two characteristics, photoluminescence (*PL*) and absorption coefficient, were compared

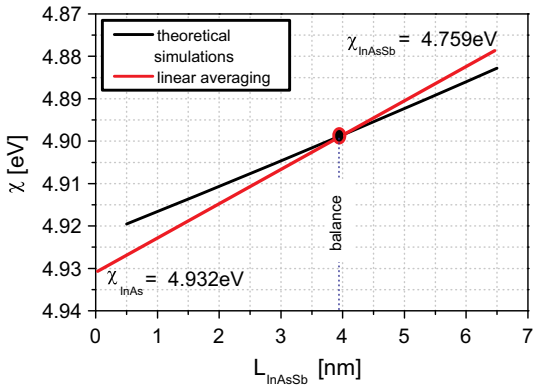

Figure 7 The theoretical simulation of the SL InAs/$InAs_{0.59}Sb_{0.41}$ electron affinity for *Sample-B* (red line—linear averaging; black line—theoretical simulations).

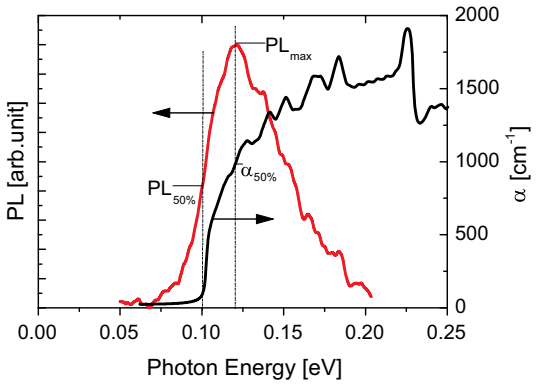

Figure 8 The simulated α and *PL* experimental data for *Sample-C* at $T = 220$ K.

(Fig. 8). This figure illustrates the difference between the energy corresponding to 100% α cutoff and the energy corresponding to 50% α cutoff, being mostly determined. It is shown that energy corresponding to the 50% *PL* maximum correlated with the width of the bandgap (the definition was described above), but the maximum of the *PL* curve agreed with the half of the absorption coefficient value allowing to draw the conclusion that the bandgap energy extracted from *PL* should be determined very carefully.

We determined bandgap based on the calculated absorption curve and *PL* measurements using the method specified above. Figure 9 shows the temperature dependence of the energy gap for *Sample-C*. The green and blue lines correspond to the theoretical calculations, while the purple squares correspond to the experimental results (reading *PL* data from the maximum and from the 50% cutoff). It is worth

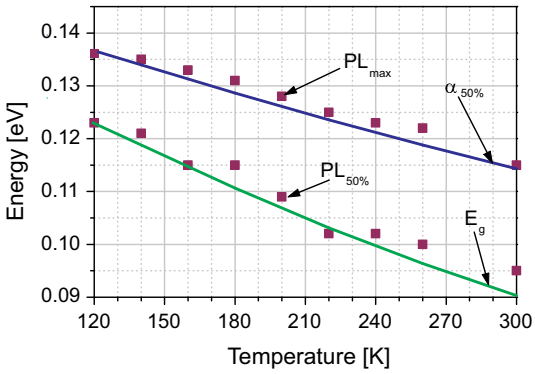

Figure 9 The simulated and measured bandgap versus temperature for *Sample-C*.

mentioning that a proper coincidence between theory and experiment was reached by accepting the temperature dependence of almost all the necessary parameters for theoretical simulations.

Table 2 presents a comparison of simulated and measured bandgap energy for the samples described in Table 1.

The detector's performance was fully confirmed by our calculations. Particularly interesting were the results for photoconductors made of *Sample-B* optimized for *VLWIR* range. After the growth, standard photolithography technique with wet-etching was used to define the active (75 × 85 μm) and contact areas of the *IR* photoconductors. The vacuum evaporation of Au/Ti electroplating was applied to fabricate ohmic contacts. At the end of the processing, the monolithic GaAs immersion lenses were formed to increase optical area of the detectors [13].

Figure 10 shows the relative responsivity characteristics (R_i) normalized to unity depending on the wavelength at the temperatures 210 K, 230 K, and 300 K. The R_i temperature dependence in arbitrary

Table 2 The theoretical and experimental data for E_g and CBO at $T = 230$ K

Sample	CBO_{theor} (eV)	$E_{g\_PL(max)}$ (eV)	$E_{g\_theor\ (50\%)}$ (eV)
A[a]	0.133	0.124	0.123
B[a]	0.148	0.078	0.075
C	0.133	0.121	0.128
D	0.133	0.191	0.174
E	0.143	0.110	0.118
F[a]	0.138	0.119	0.117
G[a]	0.143	0.118	0.111

[a]Strain-balanced samples

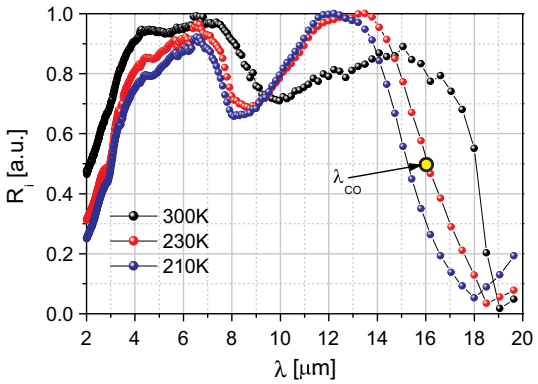

Figure 10 The normalized responsivity characteristics (experimental data) at temperatures: 210 K, 230 K and 300 K for *Sample-B*.

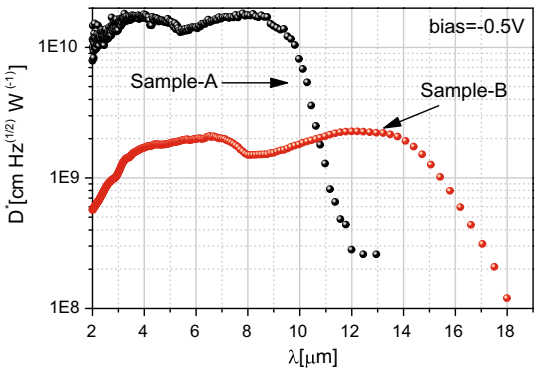

Figure 11 The experimental data D^* characteristics at $T = 230$ K for the *Sample-A* and *Sample-B*.

units was presented to show the cutoff wavelength changes versus temperature. The 50% cutoff could be then estimated from this figure. For example, at the temperature $T = 230$ K cutoff wavelength was $\lambda_{CO} \approx 16$ μm (corresponding to energy of 0.0775 eV). Comparing these data with the previous results (estimated convergence of the energy gap by photoluminescence measurement and theoretical simulations), we saw a fairly high agreement of the theory and experimental data. At 300 K, c–$1h_1$ transitions were more decisive than c–hh_1, whereas at low temperatures the situation was reverse. Comparison of the simulated absorption coefficient (see Fig. 4, *Sample-B* at $T = 230$ K) and the experimentally measured R_i (Fig. 10) gave a good bandgap match.

Figure 11 presents the detectivity (D^*) of the two samples (*Sample-A* and *Sample-B*). It should be noted that the D^*, as well as the absorption coefficient, depend on the spectral range of the detectors. At $T = 230$ K, D^* reached $\sim 8 \times 10^9$ cm $Hz^{1/2}W^{-1}$ (*Sample-A*) and $\sim 9 \times 10^8$ cm $Hz^{1/2}W^{-1}$ (*Sample-B*) for $V = -0.5$ V. Those experimental data were similar to the one presented in [6].

Conclusions

This work presents the characterization of the T2SL absorber made of the InAs and $InAs_{1-x}Sb_x$ materials on GaAs substrate with GaSb buffer layer. In our simulations, two options were considered: when the SL layer thickness corresponded to the "strain-balanced" condition and when this requirement was not met. By the "strain-balance," we meant to achieve zero average in-plane stress in the tensile/compressively strained layer of the SL and of the buffer layer, such that no shear force was generated at the interfaces between layers of the SL. By producing the SL structures that were "strain-balanced" to the buffer layer, we eliminated the possibility of the strain and dislocations occurrence suppressing the device performance. The experimental data's confirmed our theoretical simulations. The proposed method of determining the energy gap from the composition of the PL and absorption characteristic gave results consistent with the data from the responsivity detectors characteristic.

Acknowledgments

This work has been completed with the financial support of the Grant No. TECHMATSTRATEG1/347751/5/NCBR/2017.

Compliance with ethical standards

Conflict of interest The authors declare that they have no conflict of interest.

Appendix: Choice of the SL-based materials parameters

In this appendix, material parameters of binary InAs, InSb, GaSb, and ternary $InAs_{1-x}Sb_x$ materials used in the theoretical simulation the type-2 superlattice are presented. We have tested these parameters more than once in theoretical modeling of superlattices. The obtained simulation results gave good agreement with the experimental data.

The approach for selecting the necessary parameters for $InAs_{1-x}Sb_x$ bulk material is presented in Table 3. In order to determine the $InAs_{1-x}Sb_x$ "Y" band parameter, the following equation was used:

$$Y(InAs_{1-x}Sb_x) = Y(InAs)\cdot(1-x) + Y(InSb)\cdot x - bow_Y \cdot x \cdot (1-x), \quad (5)$$

where bow_Y was a bowing for Y parameter. In special cases, another non-linear interpolation was used as described in the table below.

The description of the theoretical calculation of the conductivity band offset (CBO) was presented previously [20, 23–34]. The CBO value was defined as the difference between the energies of the subbands of the conduction band for the materials constituting the SL.

$$CBO = E_c^{0(InAsSb)} + \Delta E_c^{(InAsSb)} - \left(E_c^{0(InAs)} + \Delta E_c^{(InAs)}\right), \quad (6)$$

where E_c^0 are presented in Table 3.

$$\Delta E_c^{InAsSb(InAs)} = a_c \cdot \Delta\Omega/\Omega, \quad (7)$$

Table 3 Parameters of binary bulk materials: InAs, InSb, GaSb, and the methods for the selection of the parameters for the ternary materials $InAs_{1-x}Sb_x$

Parameter		Material			
		InAs	InSb	GaSb	$InAs_{1-x}Sb_x$
Δ_{SO} (eV)	Spin–orbit energy	0.39	0.81	0.76	Bow = 1.2
E_c^0 (eV)	Electron affinity energy	− 4.945	− 4.590	− 4.060	Not linear interpolation
E_v^0 (eV)	Valence band energy	− 5.299	− 4.764	− 4.787	Not linear interpolation
$E_{v,av}^0$ (eV)	Average valence band energy (0 K)	− 5.429	− 5.034	− 5.040	Not linear interpolation
$E_{v,vac}$ (eV)	Valence band alignment	1.39	1.75	1.78	Not linear interpolation
E_{g0} (eV)	Bandgap energy at T = 0 K	0.417	0.235	0.812	Bow = $f(T)$
Q_c	Fractional conduction band offset	2.24	0.92	–	Not linear interpolation
Q_v	Fractional valence band offset	− 1.24	0.08	–	Not linear interpolation
m_e^*/m_0	Electron effective mass	0.026	0.014	0.039	Bow = $f(T)$
γ_1	Luttinger parameters	20.0	34.8	13.4	Not linear interpolation
γ_2		8.5	15.5	4.7	Not linear interpolation
γ_3		9.2	16.5	6.0	Not linear interpolation
D^{001}	Constant	1.088	1.080	0.910	Not linear interpolation
G^{001} (Mbar)	Shear modulus	1.587	1.261	1.891	Not linear interpolation
a_v (eV)	Deformation potentials (constants)	1.00	0.36	0.79	Linear interpolation
a_c (eV)		− 5.08	− 6.94	− 6.85	Linear interpolation
b (eV)		− 1.8	− 2.0	− 2.0	Linear interpolation
$a_c - a_v$		− 6.08	− 7.3	− 7.64	Linear interpolation
a_0[Å]	Lattice constant at T = 300 K	6.0583	6.4794	6.0959	Linear interpolation
C_{11} (GPa)	Elastic constants	83.2	68.47	88.42	Linear interpolation
C_{12} (GPa)		45.26	37.35	40.26	Linear interpolation
C_{44} (GPa)		39.59	31.11	43.22	Linear interpolation

a_c is the conduction band deformation potential and $\Delta\Omega/\Omega = \epsilon_{xx} + \epsilon_{yy} + \epsilon_{zz}$.

In our case, the stresses in the xx, yy, and zz directions were referenced to the GaSb buffer layer. For example, at the temperature $T = 300$ K the stresses for InAs/GaSb system were assumed by:

$$\epsilon_{xx}^{\mathrm{InAs}} = \epsilon_{yy}^{\mathrm{InAs}} = a_{\mathrm{GaSb}}/a_{\mathrm{InAs}} - 1 = 6.0959/6.0583 - 1 = 0.00621,$$
$$\epsilon_{zz}^{\mathrm{InAs}} = -D_{\mathrm{InAs}}^{001} \cdot \epsilon_{xx}^{\mathrm{InAs}} = -1.088 \cdot 0.00621 = -0.00671,$$

where $D^{001} = -2 \cdot C_{12}/C_{11}$.

$$\Delta\Omega/\Omega = 0.00621 + 0.00621 - 0.00671 = 0.00571.$$

The similar calculations for the ternary $InAs_{1-x}Sb_x$ were performed. In order to calculate the lattice constant of the ternary compound, the linear dependence of the lattice constants of binary materials InAs: $a = a_0 + 2.74 \times 10^{-5} \times (T - 300)$ and InSb: $a = a_0 + 3.48 \times 10^{-5} \times (T - 300)$ was used.

The bandgap for ternary $InAs_{1-x}Sb_x$ $(1 > x > 0)$ was determined based on binary compounds InAs and InSb according with Eq. (5). The temperature dependencies for binary compounds InAs: $E_g = E_{g0} - 2.76 \cdot 10^{-4} \cdot \frac{T^2}{(T+93)}$ and InSb: $E_g = E_{g0} - 3.20 \cdot 10^{-4} \cdot \frac{T^2}{(T+170)}$ were used. It should be noted that, the bowing parameter, bow_{E_g}, was temperature dependent, too. For example, at the $T = 0$ K, the bowing parameter was 0.9486 eV, and at the $T = 300$ K, this parameter equaled 0.67 eV [35–38]. This dependence could be approximately represented by the linear equation. We wanted to point out the fact that the bowing parameter bow_{Eg} was the sum of the bowing parameters for the electron affinity energy and the bowing parameters for the valence band energy.

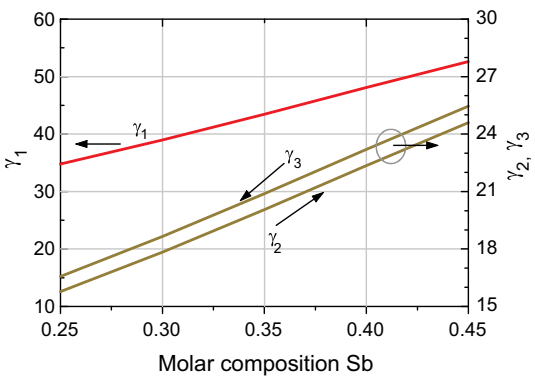

Figure 12 The Luttinger parameters versus the Sb molar composition.

The partition ratios of the band-edge discontinuities "fractional band offsets" Q_c and Q_v were important parameters for assessing the conductivity and valence band. Moreover, the fulfillment of the $Q_c + Q_v = 1$ condition was important.

The temperature dependence of the electron mass and heavy/light hole mass in bulk materials was estimated by change in the energy gap with temperature [39]. The Table 3 shows masses at temperature $T = 0$ K.

In the case of SL optical properties simulation, the Luttinger coefficients (γ_1, γ_2, and γ_3) were believed to be important parameters [12, 21, 22, 30]. These coefficients were related to the effective masses of holes (light and heavy), bandgap, and spin–orbit energies. Figure 12 shows the theoretical calculations of the Luttinger coefficients versus the Sb molar composition (x_{Sb}).

Since we were interested in a specific x_{Sb} = 0.25-0.45, the whole range of dependence (from 0 to 1) was not presented. The results shown in Fig. 12 directly indicated that in this range, Luttinger parameters were nearly linear. Such assumption of the linear dependence of the Luttinger coefficients was not allowed when calculating ternary $InAs_{1-x}Sb_x$ in the whole range $0 < x_{Sb} < 1$. In order improve the readability of Fig. 12, the γ_1 coefficient was presented in relation to the left, while γ_2, γ_3 to the right axis. The difference between the coefficients γ_2 and γ_3 did not exceed one.

References

[1] Smith DL, Mailhiot C (1987) Proposal for strained type II superlattice infrared detectors. J Appl Phys 62:2545–2548

[2] Rogalski A, Kopytko M, Martyniuk P (2017) InAs/GaSb type-II superlattice infrared detectors: three decades of development. Proc SPIE. https://doi.org/10.1117/12.2272817

[3] Rogalski A, Martyniuk P, Kopytko M (2017) InAs/GaSb type-II superlattice infrared detectors: future prospect. Appl Phys Rev 4:031304. https://doi.org/10.1063/1.4999077

[4] Yang RQ, Huang W, Li L, Lei L, Massengalea JA, Mishima TD, Santos MB (2018) Gain and resonant tunneling in interband cascade IR photodetectors. Proc SPIE. https://doi.org/10.1117/12.2289121

[5] Kim HS, Cellek OO, Lin Z-Y, He Z-Y, Zhao X-H, Liu S, Li H, Zhang Y-H (2012) Long-wave infrared nBn

photodetectors based on InAs/InAsSb type-II superlattices. Appl Phys Lett 101:161114. https://doi.org/10.1063/1.4760260

[6] Haddadi A, Chen G, Chevallier R, Hoang AM, Razeghi M (2014) InAs/$InAs_{1-x}Sb_x$ type-II superlattices for high performance long wavelength infrared detection. Appl Phys Lett 105:121104. https://doi.org/10.1063/1.4896271

[7] Lei L, Li L, Ye H et al (2015) Interband cascade infrared photodetectors with long and very-long cutoff wavelengths. Infrared Phys Technol 70:162–167

[8] Lei L, Li L, Ye H et al (2017) Long-wavelength interband cascade infrared photodetectors towards high temperature operation. Proc SPIE. https://doi.org/10.1117/12.2252566

[9] Haddadi A, Dehzangi A, Chevallier R, Adhikary R, Razeghi M (2017) Bias-selectable nBn dual-band long-/very long-wavelength infrared photodetectors based on InAs/$InAs_{1-x}Sb_x$/$AlAs_{1-x}Sb_x$ type-II superlattices. Sci Rep 7:3379. https://doi.org/10.1038/s41598-017-03238-2

[10] Bouarissa N, Aourag H (1999) Effective masses of electrons and heavy holes in InAs, InSb, GaSb, GaAs and some of their ternary compounds. Infrared Phys Technol 40:343–349

[11] Boucenna M, Bouarissa N (2007) Energy gaps and lattice dynamic properties of $InAs_xSb_{1-x}$. Mater Sci Eng, B 138(3):228–234

[12] Kim Y-S, Hummer K, Kresse G (2009) Accurate band structures and effective masses for InP. InAs, and InSb using hybrid functionals, Phys Rev B 80(3):035203. https://doi.org/10.1103/PhysRevB.80.035203

[13] Michalczewski K, Kubiszyn Ł, Martyniuk P et al (2018) Demonstration of HOT LWIR T2SLs InAs/InAsSb photodetectors grown on GaAs substrate. Infrared Phys Technol 95:222–226

[14] Perez J-P, Durlin Q, Cervera C, and Christol P (2018) New Ga-free InAs/InAsSb superlattice infrared photodetector. In: Proceedings of the 6th international conference on photonics, optics and laser technology, pp 232–237

[15] Webster PT, Shalindar AJ, Riordan NA, Gogineni C, Liang H, Sharma AR, Johnson SR (2016) Optical properties of InAsBi and optimal designs of lattice-matched and strain-balanced III-V semiconductor superlattices. J Appl Phys 119(22):225701. https://doi.org/10.1063/1.4953027

[16] Polly SJ, Bailey CG, Grede AJ, Forbes DV, Hubbard SM (2016) Calculation of strain compensation thickness for III–V semiconductor quantum dot superlattices. J Cryst Growth 454:64–70

[17] Bailey CG, Hubbard SM, Forbes DV, Raffaelle RP (2009) Evaluation of strain balancing layer thickness for InAs/GaAs quantum dot arrays using high resolution x-ray diffraction and photoluminescence. Appl Phys Let 95(20):203110. https://doi.org/10.1063/1.3264967

[18] Ekins-Daukes NJ, Kawaguchi K, Zhang J (2002) Strain-balanced criteria for multiple quantum well structures and its signature in X-ray rocking curves. Cryst Growth Des 2(4):287–292

[19] Hazbun R, Bhargava N, Rodriguez-Toro VA et al (2015) Theoretical study of the effects of strain balancing on the bandgap of dilute nitride InGaSbN/InAs superlattices on GaSb substrates. Infrared Phys Technol 69:211–217

[20] Livneh Y, Klipstein PC, Klin O, Snapi N, Grossman S, Glozman A, Weiss E (2012) k-p model for the energy dispersions and absorption spectra of InAs/GaSb type-II superlattices. Phys Rev B 86(23):235311. https://doi.org/10.1103/PhysRevB.86.235311

[21] Manyk T, Michalczewski K, Murawski K, Martyniuk P, Rutkowski J (2019) InAs/InAsSb strain-balanced superlattices for longwave infrared detectors. Sensors 19(8):1907. https://doi.org/10.3390/s19081907

[22] Birner S (2011) Modeling of semiconductor nanostructures and semiconductor-electrolyte interfaces. Ph.D. dissertation, Universität München

[23] Chuang ShL (1995) Physics of optoelectronic devices. Wiley, New York

[24] Van de Walle CG (1989) Band lineups and deformation potentials in the model-solid theory. Phys Rev B 39(3):1871–1883

[25] Lawaetz P (1971) Valence-band parameters in cubic semiconductors. Phys Rev B 4(10):3460–3467

[26] Harrison JW, Hauser JR (1976) Alloy scattering in ternary III-V compounds. Phys Rev B 13(12):5347–5350

[27] Paskov PP (1997) Refractive indices of InSb, InAs, GaSb, $InAs_xSb_{1-x}$, and $In_{1-x}Ga_xSb$: effects of free carriers. J Appl Phys 81(4):1890–1898

[28] Yu PY, Cardona M (2010) Fundamentals of semiconductors: physics and materials properties, 4th edn. Springer, Heidelberg

[29] Wei S-H, Zunger A (1998) Calculated natural band offsets of all II–VI and III–V semiconductors: chemical trends and the role of cation d orbitals. Appl Phys Let 72:2011–2013

[30] Vurgaftman I, Meyer JR, Ram-Mohan LR (2001) Band parameters for III–V compound semiconductors and their alloys. J Appl Phys 89:5815–5875

[31] Christol P, Bigenwald P, Wilk A et al (2000) InAs/InAs(P, Sb) quantum-well laser structure for the mid-wavelength infrared region. IEE Proc: Optoelectron 147(3):181–187

[32] Cardona M, Christensen NE (1987) Acoustic deformation potentials and heterostructure band offset in semiconductors. Phys Rev B 32(12):6182–6194

[33] Webster PT, Riordan NA, Liu S, Steenbergen EH, Synowicki RA, Zhang Y-H, Johnson SR (2015) Measurement of InAsSb bandgap energy and InAs/InAsSb band edge

positions using spectroscopic ellipsometry and photoluminescence spectroscopy. J Appl Phys 118:245706. https://doi.org/10.1063/1.4939293

[34] Wei S-H, Zunger A (1995) InAsSb/InAs: a type-I or a type-II band alignment. Phys Rev B 52(16):12039–12044

[35] Cripps SA, Hosea TJC, Krier A et al (2007) Midinfrared photoreflectance study of InAs-rich InAsSb and GaInAsPSb indicating negligible bowing for the spin orbit splitting energy. Appl Phys Let 90(17):172106. https://doi.org/10.1063/1.2728752

[36] Fang ZM, Ma KY, Jaw DH, Cohen RM, Stringfellow GB (1990) Photoluminescence of InSb, InAs, and InAsSb grown by organometallic vapor phase epitaxy. J Appl Phys 67(11):7034–7039

[37] Lackner D, Steger M, Thewalt MLW, Pitts OJ, Cherng YT, Watkins SP, Plis E, Krishna S (2012) InAs/InAsSb strain balanced superlattices for optical detectors: material properties and energy band simulations. J Appl Phys 111:034507. https://doi.org/10.1063/1.3681328

[38] Steenbergen EH, Nunna K, Ouyang L, Ullrich B, Huffaker DL, Smith DJ, Zhang Y-H (2012) Strain-balanced InAs/$InAs_{1-x}Sb_x$ type-II superlattices grown by molecular beam epitaxy on GaSb substrates. J Vac Sci Technol B Nanotechnol Microelectron Mater Proc Meas Phenomena 30(2):02B107. https://doi.org/10.1116/1.3672028

[39] Adachi S (2005) Properties of group – IV, III-V and II-VI Semiconductors. Wiley, London